Journal of Materials Chemistry A

PAPER

View Article Online
View Journal | View Issue

Cite this: J. Mater. Chem. A, 2018, 6, 22976

Omnidirectional and effective salt-rejecting absorber with rationally designed nanoarchitecture for efficient and durable solar vapour generation†

Xiaoying Song,[ab] Hucheng Song,*[b] Ning Xu,[b] Huafeng Yang,[ab] Lin Zhou,[b] Linwei Yu,[ab] Jia Zhu,[b] Jun Xu*[ab] and Kunji Chen[ab]

Harvesting solar energy as heat has shown fascinating applications for the purification of polluted or saline water to address the water scarcity issue globally. One of the current challenges is to realize highly efficient solar absorbers with simultaneous efficient omnidirectional light harvesting, salt-resistance and water extraction capability. In the present study, inspired by the natural lotus leaf, we propose a self-floating silicon–copper membrane consisting of hierarchical nanoscale hybrids with effective salt-resistant characteristics. We demonstrate its efficient absorbance (>93%) in a wide spectral range (200–2500 nm) and omnidirectional character (0° to 80°). We obtained a salt-water evaporation efficiency as high as 86% under one sun irradiation. The front surface of the membrane was free of salt accumulation in salt-water even after long-term operation and complete evaporation of water. More interestingly, a significant performance improvement of ~7.8% was achieved even after an ultra-long durability test in saltwater up to 310 days, which is attributed to the formation of a salt-induced robust super-hydrophilic interface layer on the water-pumping structure, thus enabling more efficient evaporation. The present hierarchical nanostructure design offers highly efficient solar photo-thermal conversion in wide angles and an excellent salt-rejecting technique, which can be easily recycled for highly efficient and stable solar vapour generation.

Received 21st August 2018
Accepted 18th October 2018

DOI: 10.1039/c8ta08138g

rsc.li/materials-a

Introduction

Harvesting and conversion of solar energy are considered as one of the most promising strategies to meet the ever-growing global demand of inexhaustible and ecofriendly energy.[1–3] Among the various strategies, the use of solar-driven steam generation devices, as an attractive approach to address energy and water scarcity issues globally, has been widely investigated.[4–6] In principle, ideal photo-thermal materials must have efficient and broad solar spectrum absorption, which is the most critical step for desalination. Therefore, engineering black absorbers were explored for highly efficient solar vapour generation, including metal plasmonic nanoparticles, carbon-based materials and other materials.[7–13] In pursuit of high photothermal efficiency, a heat localization concept was subsequently proposed by Chen's group and applied to obtain more efficient steam generation.[14] Ni *et al.* recently demonstrated a relatively high steam temperature up to 100 °C under one sun irradiation by a floating solar receiver made of inexpensive bubble wrap.[15] The further development of solar steam generation devices includes polypyrrole-coated stainless steel mesh,[16] black titanium oxides,[10,17] floatable carbon spheres,[18] plasmonic metal NPs,[11,19] and copper-based,[20] graphene-based[21–25] and wood-based membranes[26,27] as well as hierarchical nanostructured gels.[13] As representative works, Zhu *et al.* reported plasmonic metal-NP enhanced broadband absorbers *via* the three-dimensional (3D) self-assembly of multiscale structured metal (Al and Au) NPs, which overcome the inherently narrow absorption bandwidth of plasmonic metal NPs, demonstrating efficient broadband absorption (>96%, 200–2500 nm) and about 60% photothermal efficiency under one sun irradiation.[11,19] However, plasmonic material absorbers usually require a concentrating system with an optical concentration of 10–1000× for highly efficient steam generation, which are expensive ($200 per m^2).[28] Owning to their excellent light absorption and thermal conductivity properties, light carbon-based (especially graphene-based) materials have been exploited as highly efficient solar vapour generation membranes without optical concentration.[7,21–23,26,27,29] For example, Hu *et al.* reported a graphene-oxide/carbon nanotube aerogel that exhibited a ~83% photothermal conversion efficiency under

[a]School of Electronics Science and Engineering, Jiangsu Provincial Key Laboratory of Advanced Photonic and Electronic Materials, Nanjing University, Nanjing 210093, China. E-mail: hcsong@nju.edu.cn; junxu@nju.edu.cn

[b]National Laboratory of Solid State Microstructures/Collaborative Innovation Center of Advanced Microstructures, College of Engineering and Applied Sciences, Nanjing University, Nanjing 210093, China

† Electronic supplementary information (ESI) available. See DOI: 10.1039/c8ta08138g

one sun irradiation due to its effective broadband absorption (~92%) and good heat localization property.[21] Zhu *et al.* designed a solar steam generation device composed entirely of natural wood with a carbonized top, which exhibited natural advantages in the extraction of water, showing an efficient solar steam generation efficiency of ~65% under one sun-irradiation.[26] To further realize effective energy confinement, Yu *et al.* recently prepared porous gels with hierarchical water pathways, in which a record vapour generation efficiency up to 94% was achieved under one sun irradiation.[13]

Most of these studies have demonstrated relatively high evaporation efficiencies even under one sun irradiation, but the reported solar energy photothermal conversion capability of absorbers only occurs at an incident angle of sunlight approximately perpendicular to the absorber surface. However, sunlight irradiates the surface of absorbers along all directions and most of the grazing light is lost. Ren *et al.* suggested that the absorption capability of grazing light in hierarchical graphene (h-G) foam could be improved to some extent by secondary nanosheet structures grown on the three-dimensional (3D) skeleton, which demonstrated about 85% light absorption efficiency.[22] However, currently, the omnidirectional photothermal conversion capability of absorbers in extracting freshwater from seawater remains a significant and poorly studied challenge for solar vapour devices. In addition, the durability of absorbers without salt accumulation has become the most critical challenge for the long-term use and further application of solar vapour generation devices, which must be addressed in current research.[30–32] Seawater contains 3–3.5 wt% total dissolved salts (NaCl and $CaCO_3$). In most of the previous solar photothermal devices, salt may clog the channels for water pumping and vapor escape and even further accumulate on the light-receiving surface during the evaporation process.[31] This salt-covered surface will sacrifice light harvesting capability, and prevent water pumping and vapor transfer, ultimately deteriorating the evaporation performance and limiting the long-term use of the devices. In addition, saline (or seawater) conditions usually corrode the structure of membranes,[30] and this effect has been poorly studied for solar vapour generation. Therefore, the stability and durability issues of absorbers need to be addressed before solar evaporation structures can be utilized competitively for solar vapour generation.

Silicon constitutes 28% of the Earth's mass. Its high abundance, lack of toxicity and low cost coupled with its unique electrical, optical and thermal properties make silicon a fascinating prospect among the semiconductors for converting sunlight into light, heat and electricity. In particular, three-dimensional nanowire (3D NW)-structured silicon has shown huge potential for efficiently harvesting solar energy.[33] Meanwhile, this NW-architecture also exhibits a super-hydrophobic surface, which is helpful for improving the stability of solar vapour generation devices.[17,34] Herein, a highly efficient, durable and self-floating hierarchical copper–silicon (HCS) nanoscale membrane was created by mimicking the marvellous hierarchical micro-/nanostructures existing in nature such as lotus leaves, as shown in Fig. 1a. In this design, the interconnected micro-pores (Fig. 2g) embedded in the layer-structured copper foam (CF, Fig. 2h), as hierarchical water pathways, can constrain the water distribution to the near surface of the LRS, ensuring efficient water supply and vapor

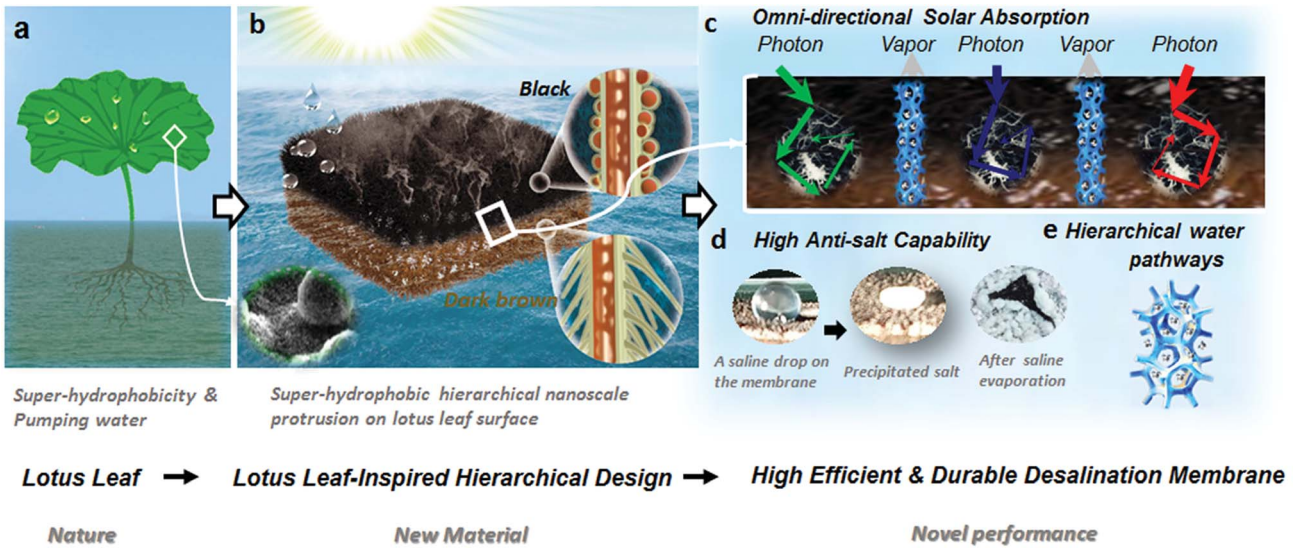

Fig. 1 Lotus leaf-inspired hierarchical nanoscale design for solar desalination. (a) Schematic demonstrating the self-cleaning capability of the lotus leaf, which grows in mud, yet is never contaminated. (b) Lotus leaf-inspired hierarchical nanoscale design of copper–silicon nanowires porous membrane for solar desalination. The black HCS NP/NW structures act as an efficient 3D light-receiving surface to harvest sunlight. The root-like HCS NW/NW structures as a water-pumping surface are in contact with the top surface of the water. (c) Omnidirectional solar light harvesting of the HCS NW gradient structure, which is then converted into thermal energy and heats up the seawater at interface, where the hierarchical porous channels enable efficient water-pumping and liquid–vapor generation close to the air–water interface. (d) Optical photographs showing the excellent anti-salt capability of the HCS NW porous membrane. (e) Hierarchical water pathways of the HCS NW porous membrane, which constrain the water distribution to the near top-surface of the membrane.

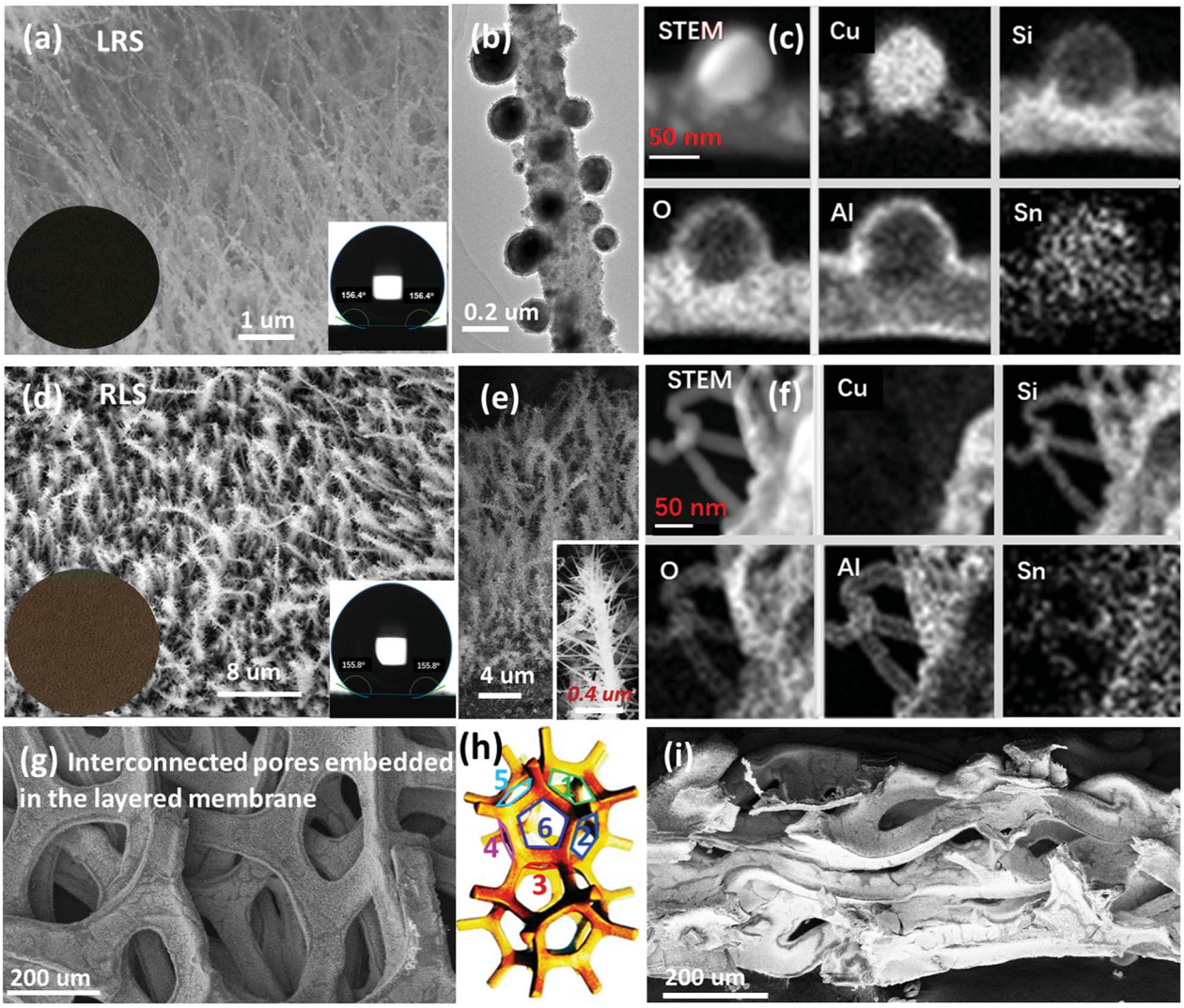

Fig. 2 Morphology and structural characterization. (a) SEM image, photograph and the contact angle of the black light-receiving surface (LRS) with Al_2O_3-coated Cu NP/Cu–Si nanowire hierarchical structures. (b and c) TEM and STEM images, respectively, and corresponding element EDX mappings of LRS with a single Al_2O_3-coated Cu NP/Cu–Si nanowire structure. (d) SEM image, photograph and the contact angle of the dark brown water-pumping surface with hierarchical Al_2O_3-coated c-SiNW/Cu–Si nanowire structures. (e) Cross-section SEM image of the root-like water-pumping surface and corresponding high-resolution SEM image of RLS with a single Al_2O_3-coated c-Si NW/Cu–Si NW structure. (f) STEM image and corresponding element EDX mappings of the single Al_2O_3-coated c-Si/Cu–Si nanowire hierarchical structure. (g) Low-magnification SEM image of the HCS NW porous membrane with interconnected micro-pores and hierarchical channels for water pumping. (h) Schematic diagram of the hierarchical water pathways, where the water (for example, flux 6) can be pumped from the nearest five passages (flux 1 to flux 5). (i) Cross-section SEM image of the HCS NW porous membrane demonstrating expedited water extraction by the hierarchical and interconnected micro-pores embedded in the layer-structured membrane.

generation (Fig. 1c). The HCS NW gradient structure (consisting of black NP/NW and dark brown NW/NW structures) was prepared on porous CF (Fig. 1b). Furthermore, the super-hydrophobic black NP/NW structure (Fig. 1b and 2a) as an LRS causes the membrane to naturally float on the water and the dark brown root-like NW/NW structure as the water-pumping surface is in contact with the top surface of the seawater (Fig. 1b and 2d). Optically, such unique hierarchical-NW gradient structure guarantees highly efficient and broad-band solar absorption at an arbitrary incident angle, as shown in Fig. 1c, *via* (1) light trapping effect of the 3D NW gradient network, (2) multiple interaction between light and hierarchical nanowires and (3) visible light enhancement of plasmonic metal nanoparticle structure. In addition, this hierarchical metal/semiconductor nanoscale design could result in a considerable enhancement in the light-introduced temperature increase and solar-thermal energy conversion efficiency.[35] Importantly, the membrane exhibits both a super-hydrophobic light-receiving surface (SLRS) and super-hydrophilic root-like surface (SRLS) in one single-layer structure after a change in its salt-induced wetting property (Fig. 1b). With this design, the HCS NW porous membrane exhibits a large contact surface (Fig. 1b), efficient hierarchical water supply and vapor generation channels (Fig. 1c and e), effective omnidirectional and

broad solar light absorption (Fig. 1c), as well as an effective salt-rejecting capability (Fig. 1d), resulting in a highly efficient and long-term stable desalination performance.

Fabrication and characterization of the HCS NW membrane

The membrane was prepared using a hierarchical bottom-up strategy, which included four basic processes (see ESI Fig. S1†). First, copper oxide (CuO) NWs were prepared on the porous foam substrate *via* a typical thermal oxidation process. Then, the sample was loaded into a plasma enhanced chemical vapor deposition (PECVD) system and an amorphous silicon film was deposited on the freely growing CuO NWs *via* the glow discharge deposition of SiH_4. In the next step, crystal silicon nanowires (c-Si NWs) were grafted on amorphous silicon (a-Si)-coated copper oxide (CuO) core–shell NWs *via* a typical Sn catalyzed vapor–liquid–solid (VLS) process and then a high-temperature H_2 annealing process was employed to reduce the copper-oxide/silicon complex structures. After coating an Al_2O_3 thin layer *via* atomic layer deposition (ALD), a single-layer structured Cu–Si porous membrane was obtained, which consisted of two typical NW-hierarchical structures: Al_2O_3-coated Cu NPs/Cu–Si nanowire light-receiving structures (black, LRS) and Al_2O_3-coated c-SiNW/Cu–Si nanowire root-like structures (dark brown, RLS) grown on both sides of the porous copper foam.

The detailed characterization of the hierarchical copper–silicon nanowire hybrid membrane is presented in Fig. 2. The membrane consists of two typical functional structures for solar desalination: a black light-receiving surface with a water contact of ~156° (Fig. 2a) and a dark brown root-like surface with a water contact of ~155.8° (Fig. 2d). The black light-receiving surface consists of hierarchical copper nanoparticle assembled copper–silicon nanowire structures (black, Al_2O_3-coated Cu NP/Cu–Si NW). The root-like water-pumping surface consists of crystal silicon nanowire-grafted copper–silicon nanowire structures (dark brown, Al_2O_3-coated c-Si NW/Cu–Si NW). It was noticed that the self-anchored NPs tend to be closely packed along the sidewalls of the Cu–Si alloy nanowire for the black LRS (Fig. 2a). The XRD characterization suggests that the NPs are copper (see ESI Fig. S2†), where the emergence of three sharp diffraction peaks located at 43.5°, 50.5° and 72.4° is ascribed to the strongest diffraction peaks of the copper crystalline planes.[36,37] As a common non-precious material, Cu NPs can also result in a strong plasmon hybridization effect and excitations with high-density localized surface plasmon resonances (LSPR).[38] In addition, the Cu NPs assembled on the nanowire network exhibit a multiscale structure with varying nanoscale gaps and a broad diameter range from several nanometers to ~200 nm (Fig. 2a and b). This design of multi-scale metal nanoparticle structures can broaden the absorption spectrum of the material.[9,10] The elemental profile analysis along the assembled nanoparticles and nanowire trunk clearly reveals a three-dimensional hierarchical NP/NW architecture, including an oxygen and aluminum element-coated Cu NP core, oxygen and aluminum element-coated Cu–Si alloy nanowire trunk and partial doping of tin (Fig. 2c). For the dark brown water-pumping surface, whiskered c-Si NWs (with diameters of approximately 30–80 nm) were grafted on the Cu–Si alloy nanowire trunks (delivering a diameter of approximately 180 nm), as shown in the partial enlargement in Fig. 2e. High-resolution transmission electron microscopy (HRTEM, Fig. S3†) showed the hierarchical architecture, including cubic Si NW branches along the [211] growth orientation, corresponding to $d = 0.27$ nm, and a Cu–Si alloy nanowire trunk, which includes a uniform a-Si:H shell layer and discontinuous and hollow Cu cores. This was further confirmed by the X-ray diffraction (XRD) spectra (see ESI Fig. S2†). The root-like water-pumping structure with an Al_2O_3 coating layer was further confirmed by elemental profile analysis of a single nanowire structure (Fig. 2f). Notably, a 3D hierarchical network of water pathways was established in the HCS NW membrane, where the interconnected pores (~50 μm, Fig. 2g) embedded in the 3D layered CF (~300 μm, Fig. 2h) to finally form hierarchical water pathways and vapor generation channels. As a result, water is localized the near surface of the LRS *via* the layer-structured CF with embedded interconnected micro-pores (Fig. 2i), where the water can be pumped from the nearest five passages (Fig. 2g and h), thus shorting the water-pumping pathway and ensuring expedited water extraction for solar desalination.

Broad solar absorption and efficient photo-thermal utilization

The absorption spectrum of the HCS NW porous membrane is shown in Fig. 3a, in which the black and dark brown lines correspond to the absorption spectra of the LRS (Al_2O_3-coated Cu NP/Cu–Si NW) and RLS (Al_2O_3-coated c-Si NW/Cu–Si NW), respectively. The absorption efficiency was calculated using the equation ($A = 1 - R - T$), where A is the absorption efficiency, R is the reflection efficiency and T is the transmission efficiency. As shown in Fig. 3a, the HCS NW membrane demonstrated efficient broadband absorption, where the average absorption efficiencies of the LRS and RLS exceeded 93% and 90%, respectively, in a wide wavelength rage from 200 nm to 2500 nm (see ESI Fig. S4a and S4b,† respectively). Remarkably, the LRS of the membrane demonstrated the lowest transmittance (~2.8%) and reflectance (~3.4%) at 200–2500 nm, thus effectively enabling a broad solar absorption (~93.8%). This light absorption capability is superior to that of hierarchical CuO/c-Si NW (HCOS NW), a-Si-coated CuO NW (a-Si/CuO NW) and CuO NW membranes (see ESI Fig. S4c†) as well as other Si-based materials.

This indicates that the absorption of the membrane was dramatically enhanced by the unique hierarchical nanowire structures, even though these structures were grown on the porous CF substrate (Fig. 2g). The light absorption enhancement is directly associated with the absorption property of the materials and the unique structure design of the membrane. Optically, in our design, the light could be "trapped" within the

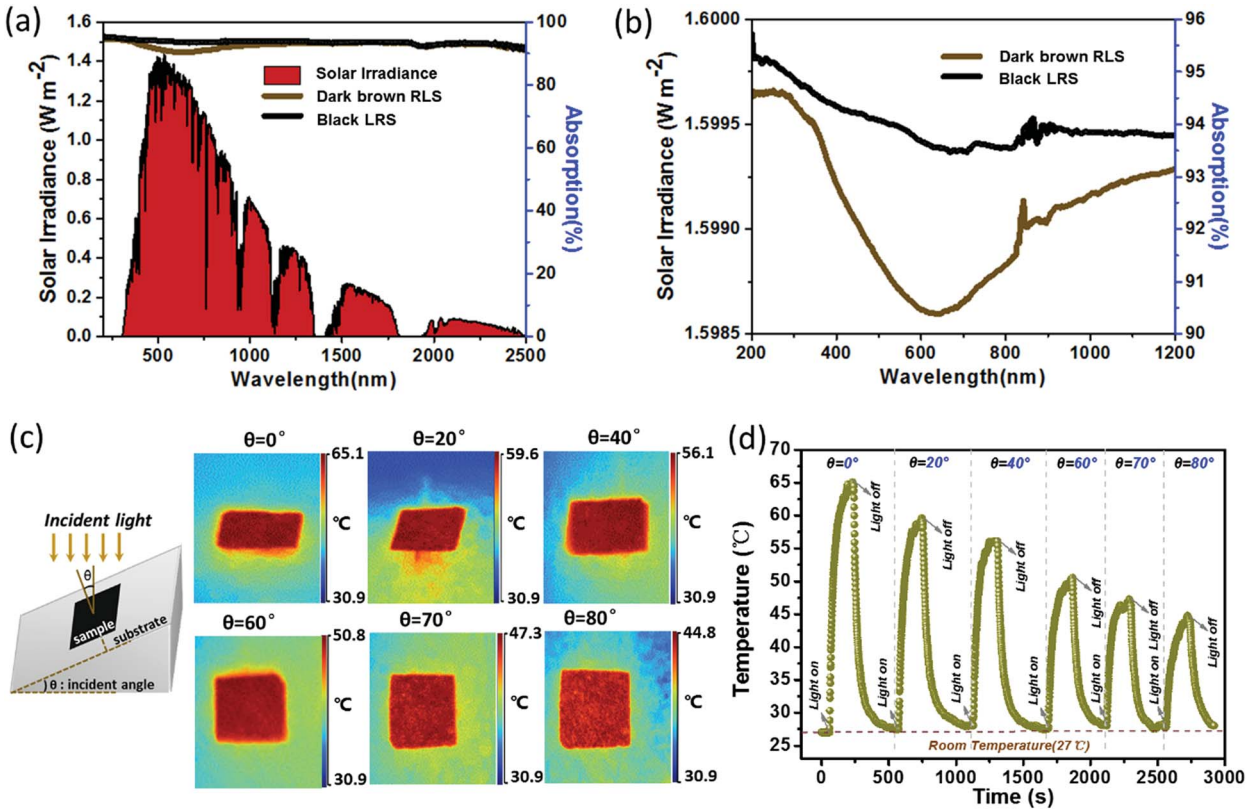

Fig. 3 Solar absorption and photothermal performance of the HCS NW membrane under one sun irradiation. (a) Absorption spectrum of LRS (black, Al_2O_3-coated Cu NP/Cu–Si NW) and RLS (dark brown, Al_2O_3-coated c-SiNW/Cu–Si NW) of the HCS NW porous membrane. (b) Corresponding local enlarged detail of (a). (c) Schematic of the sunlight incident angles and IR image of the device under one sun irradiation (AM 1.5, 1 kW m^{-2}) at 0°, 20°, 40°, 60°, 70° and 80°. (d) Temperature change in the LRS of the HCS NW membrane under one sun irradiation (with an incident angle of 0–80°) on and off cycles, where the temperature probe was placed on the center of the membrane surface.

gaps of the nanowire networks with gradient hybridization building blocks instead of bouncing off or penetrating the structure.[39,40] Meanwhile, the hierarchical nanowire gradient structure further increases the interaction length between light and the material, resulting in strong multiple internal reflections until it is absorbed completely.[33,41] Fig. 1c shows the advantages of our structure design for the maximization of omnidirectional solar light harvesting and collection. Among them, the Cu NPs, as reported in noble-metal nanostructures, show great advantages in enhancing visible and near infrared light absorption due to their strong vis-NIR absorption.[38] The local enlarged absorption spectra suggest that the black LRS with Cu NPs could more effectively absorb the broad solar spectrum (LRS, 93.8% solar-energy absorption efficiency in Fig. 3b) than the dark brown RLS. This enhancement can be attributed to the plasmonic Cu NP structure with various and broad nanoscale size gaps (Fig. 2a and b). This multiscale metal NP structure can enable a high density of hybridized LSPR, thus resulting in a broad solar absorption spectrum.[37] Meanwhile, the intrinsic Al_2O_3 coating layer can further lead to a redshift and widen the metal-based LSP resonant models (Fig. 2c).[11] Therefore, the total absorption of the membrane was significantly enhanced by the multiple interaction between light and hierarchical-NW network, plasmonic metal-NP structure and light trapping effect of its 3D NW structure. In principle, light radiation on the surface of a material is always be accompanied heat generation due to the light interaction with lattice vibrations.[42] Therefore, the photothermal properties of the membrane were also studied, especially the temperature changes under various sunlight incident angles. Fig. 3c presents a schematic of the solar-thermal imaging of the membrane, where a simulated solar light (AM 1.5) with an intensity of 1000 W m^{-2} was employed as the light source to irradiate the membrane and an intensity infrared (IR) camera was used to test the temperature of the membrane in air. The corresponding time–temperature curve (0°, 20°, 40°, 60°, 70° and 80° light incident angles) is shown in Fig. 3d. Up on one sun irradiation, the HCS NW porous membrane demonstrated an ultra-uniform temperature distribution (Fig. 3c) and gradually decreasing temperature from ~65.1 °C to ~50.8 °C (Fig. 3d) when the incident angle increased from 0° to 60°. This indicates the highly efficient light absorption and robust photothermal conversion capability of the HCS membrane for a wide range of sunlight incident angles up to 60°. Even when the incident angle was increased to 80°, an ultra-uniform photothermal temperature distribution (~44.8 °C) was obtained, which is 1.7 times room temperature (~27 °C). In addition, the light-induced temperatures increased rapidly to a steady-state value when the light was on (Fig. 3d). This clearly

suggests that the HCS NW structure can effectively convert solar energy to heat in all directions by its unique structure at a wide incident angle range from 0° to 80°, thus ensuring efficient photothermal utilization by the use of a steady-state and large surface HCS NW membrane.

Efficient and durable solar vapour generation under one sun

Fig. 4a shows the solar-driven vapour generation system composed of steam generation, condensation separation and water collection units, where the HCS NW membrane is spread on the surface of the saltwater as the solar driven interface heater to evaporate water.

In this design, the super-hydrophobic property of the HCS NW structures makes the membrane naturally float on seawater. The large surface of the HCS NW porous membrane significantly enhances the liquid–vapor change occurring close to the air–water interface. The hierarchical network of water pathways formed by the interconnected microspores (~50 μm) embedded in CF provide efficient paths for water supply, continuous flow, liquid–vapor change and stream collection. Thus, these advantages make the membrane particularly suitable for the solar evaporation process. Fig. 4b shows the mass changes of the single-layer structured HCS NW porous membrane in pure water and saline after a long-time cycle and double-layer structured device consisting of an HCS NW porous membrane and a packaging-foam based thermal insulation layer. Simulated solar light (AM 1.5) with an intensity of 1000 W m^{-2} was used and each test lasted for 1 hour. The curves clearly show that the solar-vapor conversion efficiencies of the HCS NW membrane in pure water and saline reached ~50.9% (with an evaporation rate of ~0.81 kg m^{-2} h^{-1} in Fig. 4b) and ~58.4% (with an evaporation of ~0.93 kg m^{-2} h^{-1} in Fig. 4b), respectively, after a long cycle, as shown in Fig. 4c. Further, the solar-vapor conversion efficiency increased to ~86.0% (with an evaporation rate of ~1.37 kg m^{-2} h^{-1} in Fig. S5† and the steady-state energy balance analysis in Fig. S11†) when a cloth-coated packaging-foam based thermal insulation layer (insulation foam layer and water-pumping cloth) was employed as 2D water channels (as shown in Fig. S5b†).[24] The solar-vapor conversion efficiency (η_{th}) was obtained using the following formula:

$$\eta_{th} = mh_{LV}/p_0 \quad (1)$$

where m is the mass flux, h_{LV} is the total enthalpy of the liquid–vapor phase change (2260 J g^{-1}), and p_0 is the solar irradiation power of one sun (1 kW m^{-2}).

Fig. 5 presents the long-term saline evaporation performance (average salinity of about 3.5 wt%) and contact angle (CA) test results of the HCS NW membrane. Under one sun irradiation, the total cycle numbers were maintained for about 22 cycles (15 cycles in saline, over 310 days) with each cycle sustained for over one hour. The average solar-thermal efficiency of the first 11 saline (after 3 months) tests maintained a relatively stable value up to ~50.2% (Fig. 5a, with an average evaporation rate of ~0.80 kg m^{-2} h^{-1} in Fig. 5b), which is consistent with the pure water average evaporation rate (~50%, Fig. 4b). After 12 saline cycles (corresponding to 120 days), the efficiency of the membrane increased to 55.1% (corresponding to an evaporation rate of ~0.88 kg m^{-2} h^{-1} in Fig. 5b). Meanwhile, we clearly observed that the foam sample pressed down the water surface during this saline cycle. After that, the performance of the membrane significantly improved and a final saline evaporation efficiency of 58.4% (~0.93 kg m^{-2} h^{-1} evaporation rate in Fig. 5b) was demonstrated. This result demonstrates an enhanced desalination performance (~7%) even after an ultra-long test time in saltwater (up to 310 days), which is the best among the comparable state-of-the-art systems published recently in top journals (see ESI Table S1†). Fig. 5c presents the long-term CA test results of the LRS and RLS under various environments,

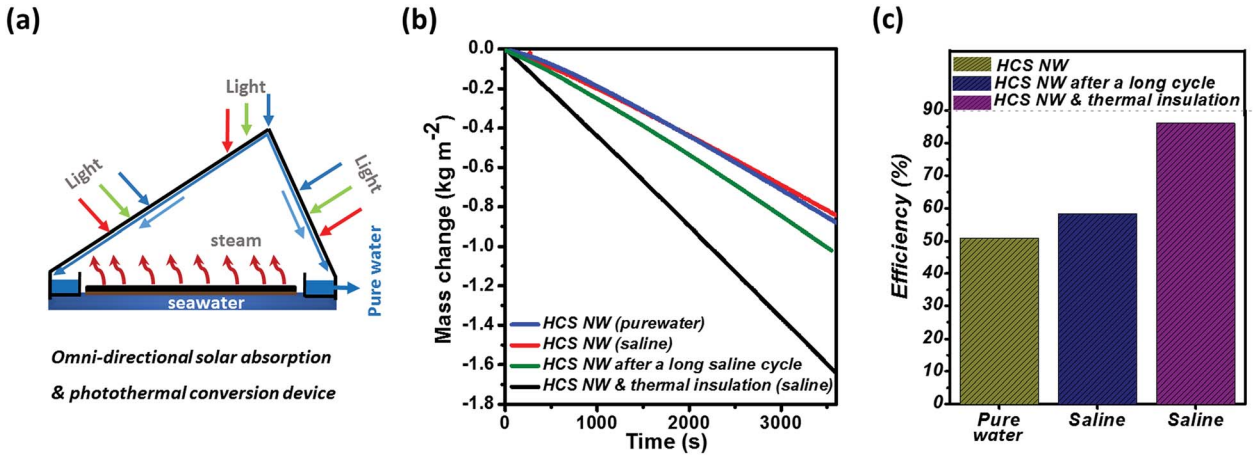

Fig. 4 Performance of the HCS NW membrane under one sun irradiation. (a) Structure of solar-vapor generation system, where the HCS NW gradient structure, as a solar vapour generation membrane, could effectively absorb an omnidirectional and broad solar spectrum. (b) Evaporation performances of the single-layer structured HCS NW porous membrane in pure water and saline at the 15th saltwater cycle, and double-layer structured device consisting of an HCS NW membrane and a packaging-foam based thermal insulation layer, in which one operating cycle lasted about 1 h. (c) Corresponding efficiencies of these structures.

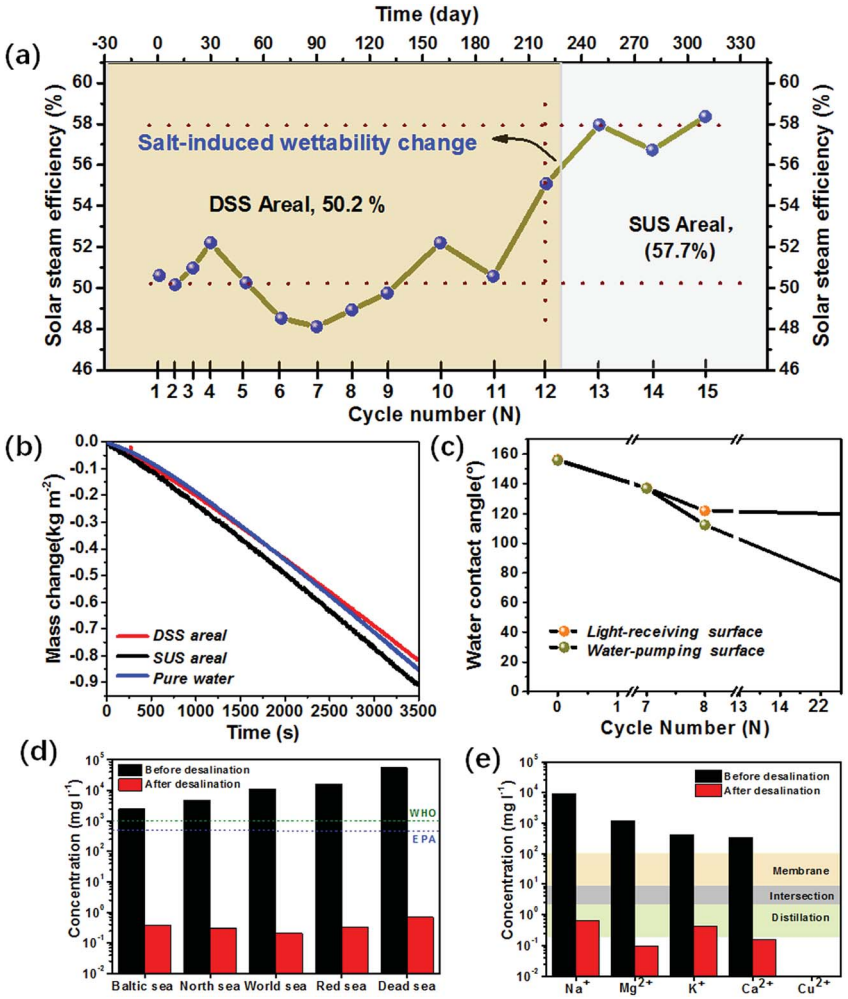

Fig. 5 Solar desalination performance of the HCS NW membrane under one sun irradiation. (a) Saline evaporation performance of the HCS NW porous membrane, where the membrane was successively cycled for 7 cycles in pure water and 15 cycles in saline for more than 310 days. Each cycle lasted about 1 h. (b) Average pure water mass change and average saline mass change of the membrane cycled in the double-side super-hydrophobic area (DSS) and super-hydrophobic/underwater super-hydrophilic areal (SUS). (c) Contact angle change in the light-receiving surface and water-pumping surface of the membrane under various environments, including initial sample, after 7 cycles in pure water and then followed by 1 cycle and 15 cycles in saline. (d) Salinity of five critical seawater samples before and after desalination using the HCS NW membrane. (e) Measured concentrations of five primary ions in an actual seawater sample before and after desalination. The orange shaded area refers to the overall typical salinity achieved by the traditional membrane desalination process and the green shaded area refers to the overall typical salinity achieved by the traditional distillation desalination process.

including initial sample (0 cycle), 7th pure water cycle and 15th saline cycle. It is clear that the initial HCS NW membrane exhibited double-sided super-hydrophobic properties with a CA greater than 155° for LRS and RLS. After 7 cycles in pure water, the CA of both surfaces slightly decreased to about 137°. During the following saline cycle, the LRS of the membrane maintained its hydrophobic property with the contact angle decreasing from 121° in the 1st saline cycle to 116° in the 15th saline cycle. However, the CA of the RLS rapidly decreased from 112° in the 1st saline cycle to 0° in the 15th saline cycle, which indicates a surface wetting change in the RLS from super-hydrophobicity to super-hydrophilicity after the saline cycles. This wettability-inversion of the RLS will result in an enhancement in water flux and enable more efficient evaporation. Meanwhile, is also suggested that the LRS of the membrane retained its robust super-hydrophobic feature during the long-time saline cycles. This feature makes the membrane naturally long-term float on water. According to the above results, the complete saline cycle process of the membrane occurs on two typical areas, which can be defined as a double-sided super-hydrophobic areal (DSS, Fig. 5c) and super-hydrophobic/underwater super-hydrophilic areal (SUS, Fig. 5c) area. To evaluate the solar desalination result of the HCS NW membrane, five typical critical seawater samples were used and carefully tracked by conductivity coupled plasma spectroscopy (ICP-OES, OPTIMA 5300 DV, 0.1 mg L^{-1} in accuracy), including the Baltic Sea (0.8 wt%), the North Sea (~1.4 wt%), the World Ocean (3.5 wt%), the Red Sea (4.1 wt%) and the Dead Sea (10 wt%). It was clearly observed that the salinities of the five critical seawater samples strikingly decreased (by ~four orders of magnitude, as shown in Fig. 5d) and were approximately two orders of magnitude below the drinking water standards defined by the World Health

Organization and the US Environmental Protection Agency.[11] Further, seawater from the Bohai Sea (from Xiamen, China) was used for desalination by the HCS NW membrane. After desalination, the concentrations of all four primary ions (Na^+, Mg^{2+}, K^+ and Ga^+) were significantly reduced, which were below the values typically obtained by membrane-based (10–500 mg L^{-1}) and distillation-based (1–50 mg L^{-1}) seawater desalination techniques.[11] In addition, we observed that the concentrations of Cu ions were below the detection limit of ICP-OES (0.1 mg L^{-1}) after desalination, indicating the successful production of potable water using our HCS NW membrane under solar irradiation.

Mechanism for efficient and durable solar water evaporation

Actually, the wettability-inversion of a membrane is closely related to the surface property of its materials, which may be

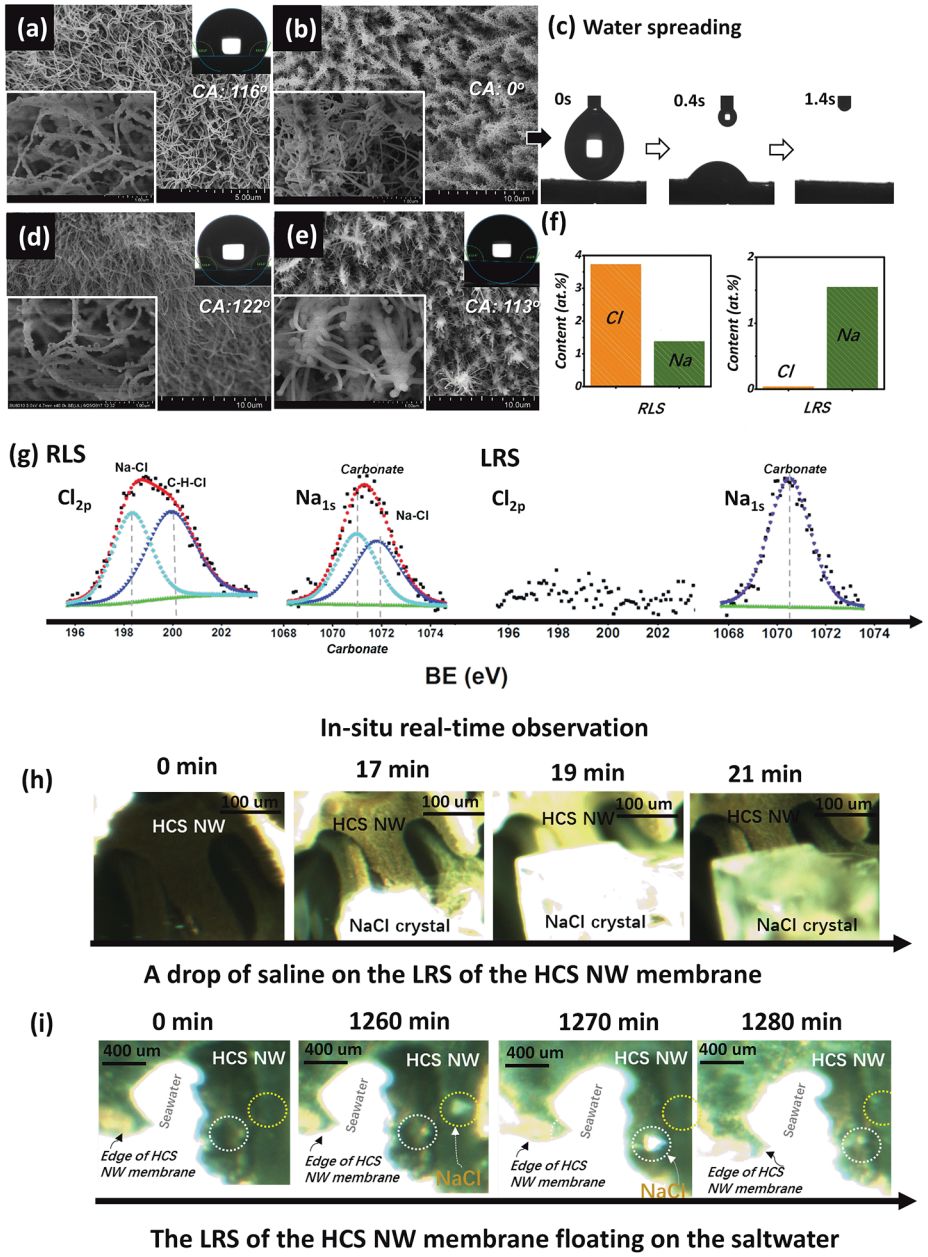

Fig. 6 Morphology and contact angle characterization of HCS NW porous membrane after cycles in 3.5 wt% NaCl solution. (a and d) SEM and CA of the LRS (Al_2O_3-coated Cu NP/Cu–Si NW) and RLS (Al_2O_3-coated c-Si NW/Cu–Si NW) of the HCS NW membrane after one saline cycle, respectively. (c) Photograph of the dynamic measurements of water spreading for the RLS of (b). (b and e) SEM and CA of the LRS and RLS after 15 saline cycles, respectively. (f) Corresponding surface element content of Na and Cl of the LRS and RLS characterized by XPS after long saline cycles. (g) High-resolution XPS spectra (Na 1s and Cl 2p) of the RLS and the LRS after long saline cycles. (h) *In situ* real-time observation of a drop saline on the surface of the HCS NW membrane under Xe-lamp irradiation. (i) *In situ* real-time observation of the surface of the HCS NW membrane floating on the saline under Xe-lamp irradiation.

caused by the evolution of its structure[34] and the formation of hydrophilic groups.[29] Thus, to understand the surface property evolutions of the HCS NW membrane during solar desalination, its morphology and surface chemical composition were characterized after the saline cycles. The morphologies of both the LRS (Fig. 6a) and RLS (Fig. 6b) showed little change after a long cycle (7 pure water and 15 saline cycles) compared with the membrane before cycling (Fig. 2a and d) and after one saline cycle (Fig. 6d and e), respectively. This indicates the robustness of the HCS NW membrane during the durability test with saline. Highly ceramic-like particles were observed, which were mainly anchored on the surface of the Cu–Si trunk of the RLS (see in partially enlarged detail in Fig. 6b). Both sodium (Na, ~1.4 at%) and chlorine (Cl, ~3.7 at%) were detected on the surface of the RLS after long saline cycles. However, only Na (1.5 at%) was found on the surface of the LRS (Fig. 6f). Further, the surface composites of the membrane were characterized by high-resolution X-ray photoelectron spectroscopy (XPS) analysis (Fig. S6a and S6b†). It was observed that the RLS (Fig. 6g) soaked in saline was largely composed of carbonates, hydrocarbons and sodium chloride (Fig. S6a and S6b†).[43–46] Most of these components are hydrophilic.[29,47] Thus, the formation of these components can be attributed to the formation of NaCl on the RLS and chemical/photochemical reaction occurring on the RLS of the membrane in the system including H_2O, CO_2 and solar light irradiation. Notably, both NaCl (Na 1s peak located at ~1072 eV) and Na_2CO_3 (at ~1070.8 eV) were detected on the surface of the RLS (Fig. 6g). However, only Na_2CO_3 (at ~1070.6 eV) was observed on the surface of the LRS of the HCS NW membrane and no chlorine signal was found (Fig. 6g). This indicates that the HCS NW gradient structure could act as an ion selective membrane to allow sodium cations (Na^+) to pass through and meanwhile inhibit chloride anions (Cl^-) during solar desalination. As the result, the NaCl-induced surface wetting change (from super-hydrophobic to super-hydrophilic) is only favorable for the RLS. This is also thought to mainly contribute to the substantially increased evaporation efficiency and the robustness/stability of the HCS NW membrane after long-time saline cycles. Further, *in situ* optical microscopy was employed to study the salt-rejecting capability of the HCS NW membrane under Xe-lamp irradiation. Fig. 6h clearly shows the water shrinkage and salt precipitation process of a saline drop on the HCS NW membrane (LRS) under irradiation. The precipitated salt-crystal was supported by the HCS NWs instead of penetrating into the interior of the membrane through its interconnected micro-pores (~50 μm to ~200 μm, Fig. 2g) due to the robust and stable super-hydrophobic LRS of the HCS NW membrane (Fig. 6h and S9†). This robust and stable hydrophobic feature caused the pre-formed NaCl crystal particles (Fig. 6i, 120 min and 130 min) on the surface of the LRS to dissolve in the water in the subsequent saltwater process (Fig. 6i, 140 min), as shown by the *in situ* real-time observation on the LRS of the HCS NW membrane floating on the saline (Fig. 6i and S8†).

This may be the main reason for the failure of the salt to occupy the light-receiving surface of our membrane. This capability is superior to most solar absorbers,[21] where dense and crowded salt crystals are formed on the whole membrane during long-term solar irradiation. It is highly likely that the surface composites confer zwitterionic behavior[46] to our membrane, resulting in a robust and stable super-hydrophobic LRS, which enables effective salt-rejection and long-term stability for solar vapour generation.

Conclusions

In conclusion, an omnidirectional light absorption and effective salt-rejecting HCS NW porous membrane was prepared using a hierarchical bottom-up strategy. Our design was inspired by the natural lotus leaf, where the HCS NW gradient structures were directly grown on the 3D CF with interconnected micropores, which consists of black NP/NW light-receiving structures and root-like NW/NW water-pumping structures. This design: (1) ensures highly efficient solar harvesting in a wide spectral range and omnidirectional character *via* the strong multiple interaction between light and hierarchical-NW architecture; (2) makes the membrane enjoy both a robust super-hydrophobic LRS and a stable super-hydrophilic RLS in one single-layer structure, even after a long-time saline cycle; and (3) provides hierarchical water pathways, which can constrain the water distribution to the near surface of the LRS, thus ensuring efficient water absorption and vapor generation. As a result, this membrane could naturally float on the water surface and efficiently absorb (~93%) solar absorption in a wide spectral range (200–2500 nm) with omnidirectional character (0° to 80°), which is superior to that in most reported works. In addition, this membrane exhibits effective salt-rejection even at a high concentration of salt (20 wt%). The light-receiving surface of the membrane was free of salt accumulation in saline water even after several weeks due to the robust super-hydrophobic feature of our designed structures. A high vapour generation efficiency (~86%) was also achieved with the HCS NW membrane under one sun irradiation. The durability test result demonstrated an enhanced desalination performance (~7%) even after an ultra-long test time in saltwater (up to 310 days), which is the best among comparable state-of-the-art systems published recently in top journals (see ESI Table S1[48–52]†). This improvement is mainly attributed to the formation of a super-hydrophilic RLS after salt-induced wettability-inversion. This hierarchical nanostructured membrane offers highly efficient solar harvesting in a wide angle range and excellent salt-rejecting technology, which is easily recycled for long-term and efficient solar vapour generation.

Methods

Synthesis of the HCS NW porous membrane

Commercial CF (with a thickness in the range of 0.3 mm to 0.5 mm) was first soaked in hydrochloric acid for 30 min and then dried under an argon atmosphere. Copper oxide (CuO) NWs were directly prepared on the foam substrates in a conventional furnace tube by a thermal oxidation process in air atmosphere. Then, the sample was loaded in a PECVD system and an amorphous silicon (a-Si) film was coated on the CuO NW cores

at 200 °C with 5 sccm SiH_4 and 50 sccm H_2, 600 mTorr pressure and 76 mW cm^{-2} RF power density. In the next step, a tin (Sn) film (~5 nm) was prepared on the CuO/a-Si core–shell NWs using a thermal evaporation system. After that, Si NW branches were grafted on the CuO/a-Si core–shell NW trunks *via* an Sn-droplet-catalyzed VLS process at 480 °C with 5 sccm SiH_4 and 50 sccm H_2, 600 mTorr pressure, and 76 mW cm^{-2} RF power density. This was followed by annealing under an H_2 atmosphere at 600 °C for 240 min to reduce the CuO core into Cu to form the HCS NW gradient structure. Finally, a thin Al_2O_3 layer was deposited *via* thermal atomic layer deposition (ALD) using O_2 and $Al(CH_3)_3$ (TEMA) as the Al and O sources, respectively.

Optical measurements

Optical transmittance and reflectance spectra of the materials were measured in the wavelength range of 200–2500 nm with an integrating sphere model (ISR-3100) on a Shimadzu UV3600 spectrophotometer. The absorption efficiency was then calculated using the equation $A = 1 - R - T$, where A is the absorption efficiency, R is the reflection efficiency and T is the transmission efficiency.

Experimental set-up for solar desalination

The test system for the solar desalination included a solar simulator (Newport 94043A) and a high accuracy balance (Liang Ping Tech, FA2004, 0.1 mg in accuracy). The optical power on the surface of the membrane was measured by a standard solar cell (Newport 91150V) and an optical power meter (Coherent 1097901). The light-to-heat conversion temperature of the membrane was measured using a thermal infrared imager (Fluke Ti100) and a thermocouple thermometer (Bolsen, HT9815). The mass change in water was measured using a high accuracy balance and then real-time transferred to a desk computer for the evaluation of the evaporation rate and solar-thermal conversion efficiency.

Conflicts of interest

There are no conflicts to declare.

Acknowledgements

This research was partially supported financially by the National Natural Science Foundation of China (61735008), National Postdoctoral Program for Innovative Talents (BX201600067), Chinese Postdoctoral Science Foundation (179709), Postdoctoral Science Foundation of Jiangsu Province of China (1701120B), and Fundamental Research Funds for the Central Universities (0213-14380062).

References

1 M. A. Shannon, P. W. Bohn, M. Elimelech, J. G. Georgiadis, B. J. Marinas and A. M. Mayes, *Nature*, 2008, **452**, 301–310.
2 M. Elimelech and W. A. Phillip, *Science*, 2011, **333**, 712–717.
3 O. Neumann, C. Feronti, A. D. Neumann, A. Dong, K. Schell, B. Lu, E. Kim, M. Quinn, S. Thompson, N. Grady, P. Nordlander, M. Oden and N. J. Halas, *Proc. Natl. Acad. Sci. U. S. A.*, 2013, **110**, 11677–11681.
4 S. Chu, Y. Cui and N. Liu, *Nat. Mater.*, 2016, **16**, 16–22.
5 J. H. Montoya, L. C. Seitz, P. Chakthranont, A. Vojvodic, T. F. Jaramillo and J. K. Norskov, *Nat. Mater.*, 2016, **16**, 70–81.
6 H. Sharon and K. S. Reddy, *Renewable Sustainable Energy Rev.*, 2015, **41**, 1080–1118.
7 Y. Ito, Y. Tanabe, J. Han, T. Fujita, K. Tanigaki and M. Chen, *Adv. Mater.*, 2015, **27**, 4302–4307.
8 H. Ghasemi, G. Ni, A. M. Marconnet, J. Loomis, S. Yerci, N. Miljkovic and G. Chen, *Nat. Commun.*, 2014, **5**, 4449.
9 K. Bae, G. Kang, S. K. Cho, W. Park, K. Kim and W. J. Padilla, *Nat. Commun.*, 2015, **6**, 10103.
10 J. Wang, Y. Li, L. Deng, N. Wei, Y. Weng, S. Dong, D. Qi, J. Qiu, X. Chen and T. Wu, *Adv. Mater.*, 2017, **29**, 1603730.
11 L. Zhou, Y. Tan, J. Wang, W. Xu, Y. Yuan, W. Cai, S. Zhu and J. Zhu, *Nat. Photonics*, 2016, **10**, 393–398.
12 Y. M. Liu, S. T. Yu, R. Feng, A. Bernard, Y. Liu, Y. Zhang, H. Z. Duan, W. Shang, P. Tao, C. Y. Song and T. Deng, *Adv. Mater.*, 2015, **27**, 2768.
13 F. Zhao, X. Y. Zhou, Y. Shi, X. Qian, M. Alexander, X. P. Zhao, S. Mendez, R. G. Yang, L. T. Qu and G. H. Yu, *Nat. Nanotechnol.*, 2018, **13**, 489–495.
14 H. Ghasemi, G. Ni, A. M. Marconnet, J. Loomis, S. Yerci, N. Miljkovic and G. Chen, *Nat. Commun.*, 2014, **5**, 4449.
15 G. Ni, G. Li, S. V. Boriskina, H. X. Li, W. L. Yang, T. J. Zhang and G. Chen, *Nat. Energy*, 2016, **1**, 16126.
16 Z. B. Zha, X. L. Yue, Q. S. Ren and Z. F. Dai, *Adv. Mater.*, 2013, **25**, 777–782.
17 M. M. Ye, J. Jia, Z. J. Wu, C. X. Qian, R. Chen, P. G. O'Brien, W. Sun, Y. C. Dong and G. A. Ozin, *Adv. Energy Mater.*, 2017, **7**, 1601811.
18 J. G. Zhou, Z. L. Sun, M. Q. Chen, J. T. Wang, W. M. Qiao, D. H. Long and L. C. Ling, *Adv. Funct. Mater.*, 2016, **26**, 5368–5375.
19 L. Zhou, Y. L. Tan, D. X. Ji, B. Zhu, P. Zhang, J. Xu, Q. Q. Gan, Z. F. Yu and J. Zhu, *Sci. Adv.*, 2016, **2**, e1501227.
20 X. Gao, H. Y. Ren, J. Y. Zhou, R. Du, C. Yin, R. Liu, H. L. Peng, L. M. Tong, Z. F. Liu and J. Zhang, *Chem. Mater.*, 2017, **29**, 5777–5781.
21 X. Z. Hu, W. C. Xu, L. Zhou, Y. L. Tan, Y. Wang, S. N. Zhu and J. Zhu, *Adv. Mater.*, 2017, **29**, 1604031.
22 H. Y. Ren, M. Tang, B. L. Guan, K. X. Wang, J. W. Yang, F. F. Wang, M. Z. Wang, J. Y. Shan, Z. L. Chen, D. Wei, H. L. Peng and Z. F. Liu, *Adv. Mater.*, 2017, **29**, 1702590.
23 J. L. Yang, Y. S. Pang, W. X. Huang, S. K. Shaw, J. Schiffbauer, M. A. Pillers, X. Mu, S. R. Luo, T. Zhang, Y. J. Huang, G. X. Li, S. Ptasinska, M. Lieberman and T. F. Luo, *ACS Nano*, 2017, **11**, 5510–5518.
24 X. Q. Li, W. C. Xu, M. Y. Tang, L. Zhou, B. Zhu, S. N. Zhu and J. Zhu, *Proc. Natl. Acad. Sci. U. S. A.*, 2016, **113**, 13953–13958.
25 Y. J. Li, T. T. Gao, Z. Yang, C. J. Chen, W. Luo, J. W. Song, E. Hitz, C. Jia, Y. B. Zhou, B. Y. Liu, B. Yang and L. B. Hu, *Adv. Mater.*, 2017, **29**, 1700981.

26 M. W. Zhu, Y. J. Li, G. Chen, F. Jiang, Z. Yang, X. G. Luo, Y. B. Wang, S. D. Lacey, J. Q. Dai, C. W. Wang, C. Jia, J. Y. Wan, Y. G. Yao, A. Gong, B. Yang, Z. F. Yu, S. Das and L. B. Hu, *Adv. Mater.*, 2017, **29**, 1704107.
27 T. Li, H. Liu, X. Zhao, G. Chen, J. Dai, G. Pastel, C. Jia, C. Chen, E. Hitz, D. Siddhartha, R. Yang and L. Hu, *Adv. Funct. Mater.*, 2018, **28**, 1707134.
28 Ernst & Young Inc., Fraunhofer Institute for Solar Energy Projects, *Assessment of the Local Manufacturing Potential for Concentrated Solar Power (CSP) Projects*, The World Bank, Washington D.C., 2011.
29 J. Yang, Y. Pang, W. Huang, S. K. Shaw, J. Schiffbauer, M. A. Pillers, X. Mu, S. Luo, T. Zhang, Y. Huang, G. Li, S. Ptasinska, M. Lieberman and T. Luo, *ACS Nano*, 2017, **11**, 5510–5518.
30 A. Morelos-Gomez, R. Cruz-Silva, H. Muramatsu, J. Ortiz-Medina, T. Araki, T. Fukuyo, S. Tejima, K. Takeuchi, T. Hayashi, M. Terrones and M. Endo, *Nat. Nanotechnol.*, 2017, **12**, 1083–1088.
31 W. Xu, X. Hu, S. Zhuang, Y. Wang, X. Li, L. Zhou, S. Zhu and J. Zhu, *Adv. Energy Mater.*, 2018, 1702884, DOI: 10.1002/aenm.201702884.
32 G. Ni, S. H. Zandavi, S. M. Javid, S. V. Boriskina, T. A. Cooper and G. Chen, *Energy Environ. Sci.*, 2018, **11**, 1510–1519.
33 M. J. Bierman and S. Jin, *Energy Environ. Sci.*, 2009, **2**, 1050.
34 B. S. Kim, S. Shin, S. J. Shin, K. M. Kim and H. H. Cho, *Langmuir*, 2011, **27**, 10148–10156.
35 R. Jiang, B. Li, C. Fang and J. Wang, *Adv. Mater.*, 2014, **26**, 5274–5309.
36 H. Song, H. X. Wang, Z. Lin, X. Jiang, L. Yu, J. Xu, Z. Yu, X. Zhang, Y. Liu, P. He, L. Pan, Y. Shi, H. Zhou and K. Chen, *Adv. Funct. Mater.*, 2016, **26**, 524–531.
37 D. C. Johnson, J. M. Mosby, S. C. Riha and A. L. Prieto, *J. Mater. Chem.*, 2010, **20**, 1993.
38 S. Linic, U. Aslam, C. Boerigter and M. Morabito, *Nat. Mater.*, 2015, **14**, 567–576.
39 E. Garnett and P. Yang, *Nano Lett.*, 2010, **10**, 1082–1087.
40 L. Cao, J. S. White, J. S. Park, J. A. Schuller, B. M. Clemens and M. L. Brongersma, *Nat. Mater.*, 2009, **8**, 643–647.
41 X. Li, J. Yu and M. Jaroniec, *Chem. Soc. Rev.*, 2016, **45**, 2603–2636.
42 G. Liu, J. Xu and K. Wang, *Nano Energy*, 2017, **41**, 269–284.
43 L. Yi, S. Ci, S. Luo, P. Shao, Y. Hou and Z. Wen, *Nano Energy*, 2017, **41**, 600–608.
44 C. Lee, K. Oh, D. Lee, Y. Kim, H. Yoon, D.-W. Park, M. Gab Kim, K. Lee and J. Choi, *J. Phys. Chem. Solids*, 2017, **103**, 87–94.
45 B. Shen, P. J. Zuo, P. Fan, J. Yang, G. P. Yin, Y. L. Ma, X. Q. Cheng, C. Y. Du and Y. Z. Gao, *J. Solid State Electrochem.*, 2017, **21**, 1195–1201.
46 W. F. Chan, H. Y. Chen, A. Surapathi, M. G. Taylor, X. H. Shao, E. Marand and J. K. Johnson, *ACS Nano*, 2013, **7**, 5308–5319.
47 W. Zhang, Y. Zhu, X. Liu, D. Wang, J. Li, L. Jiang and J. Jin, *Angew. Chem., Int. Ed.*, 2014, **53**, 856–860.
48 N. Xu, X. Z. Hu, W. C. Xu, X. Q. Li, L. Zhou, S. N. Zhu and J. Zhu, *Adv. Mater.*, 2017, **29**, 1606762.
49 M. W. Zhu, Y. J. Li, F. J. Chen and L. B. Hu, *Adv. Energy Mater.*, 2018, **8**, 1701028.
50 G. Ni, S. H. Zandavi, S. M. Javid, S. V. Boriskina, T. Cooper and G. Chen, *Energy Environ. Sci.*, 2018, **11**, 1510–1519.
51 X. Q. Li, J. L. Li, J. Y. Lu, N. Xu, C. L. Chen, X. Z. Min, B. Zhu, H. X. Li, L. Zhou, S. N. Zhu, T. J. Zhang and J. Zhu, *Joule*, 2018, **2**, 1331–1338.
52 H. M. Song, Y. H. Liu, Z. J. Liu, M. H. Singer, C. Y. Li, A. R. Cheney, D. X. Ji, L. Zhou, N. Zhang, X. Zeng, Z. M. Bei, Z. F. Yu, S. H. Jiang and Q. Q. Gan, *Adv. Sci.*, 2018, **5**, 1800222.

